

First-in-human liver-tumour surgery guided by multispectral fluorescence imaging in the visible and near-infrared-I/II windows

Zhenhua Hu^{1,2,7}, Cheng Fang^{3,7}, Bo Li^{3,7}, Zeyu Zhang^{1,4,7}, Caiguang Cao^{1,2}, Meishan Cai^{1,2}, Song Su³, Xingwang Sun³, Xiaojing Shi^{1,2}, Cong Li^{1,2}, Tiejun Zhou³, Yuanxue Zhang³, Chongwei Chi¹, Pan He³, Xianming Xia³, Yue Chen³, Sanjiv Sam Gambhir ^{5*}, Zhen Cheng ^{5*} and Jie Tian ^{1,2,4,6*}

The second near-infrared wavelength window (NIR-II, 1,000–1,700 nm) enables fluorescence imaging of tissue with enhanced contrast at depths of millimetres and at micrometre-scale resolution. However, the lack of clinically viable NIR-II equipment has hindered the clinical translation of NIR-II imaging. Here, we describe an optical-imaging instrument that integrates a visible multispectral imaging system with the detection of NIR-II and NIR-I (700–900 nm in wavelength) fluorescence (by using the dye indocyanine green) for aiding the fluorescence-guided surgical resection of primary and metastatic liver tumours in 23 patients. We found that, compared with NIR-I imaging, intraoperative NIR-II imaging provided a higher tumour-detection sensitivity (100% versus 90.6%; with 95% confidence intervals of 89.1%–100% and 75.0%–98.0%, respectively), a higher tumour-to-normal-liver-tissue signal ratio (5.33 versus 1.45) and an enhanced tumour-detection rate (56.41% versus 46.15%). We infer that combining the NIR-I/II spectral windows and suitable fluorescence probes might improve image-guided surgery in the clinic.

Fluorescence imaging in the near-infrared window I (NIR-I, 700–900 nm) has shown many benefits, in particular, high spatial and temporal resolution^{1–7}, not offered by other imaging modalities. It has gained recognition as a powerful technique and is expected to have an important role in a variety of clinical scenarios, for example, in fluorescence image-guided surgery and diagnostic imaging^{8–12}. Besides several conventional small-molecule NIR dyes such as methylene blue, fluorescein sodium and indocyanine green (ICG), which were approved by the Food and Drug Administration for routine clinical use, many molecularly targeted fluorescence probes have been developed and are under active clinical evaluation, such as the folate receptor α -targeted fluorescent probe folate-FITC¹³, the c-MET-targeted optical probe GE-137¹⁴ and the epidermal growth factor receptor-targeted probe Cetuximab-IRDye800CW¹⁵. NIR-I fluorescence imaging is thus a promising approach for clinical applications.

Although NIR-I imaging performs better than imaging at visible wavelengths, recent advances in optical-imaging research have shown that imaging quality can be improved in living subjects by detecting in the second NIR window (NIR-II, 1,000–1,700 nm). This is mainly attributed to diminished tissue autofluorescence, reduced photon scattering and low levels of photon absorption at longer wavelengths^{16,17}. Outstanding gains in performance when using the NIR-II window include light detection across centimetres of tissue, micrometre resolution at depths of millimetres and high target-to-background contrast, all achievable in real time.

However, NIR-II imaging has not been tested in a clinical environment, mainly because of a lack of suitable imaging instruments and optical probes. Although a variety of NIR-II optical probes, including nanoparticles, organic polymers and small-molecule dyes have been developed^{18–23}, these have not been tested in clinic. Recently, the conventional NIR-I dyes ICG and IRDye800CW have been found to show tail fluorescence in the NIR-II window³⁰, and clinically used ICG has been further proved to be suitable for NIR-II imaging with high performance in small-animal models^{31,32}. These findings pave the way for the clinical translation of NIR-II imaging.

Motivated by these advances, we present the development of an integrated visible and NIR-I/II multispectral imaging instrument, and characterize its imaging performance at different infrared windows in phantom and animal studies. We also report the first-in-human study of visible, NIR-I and NIR-II multispectral imaging in 23 patients with liver cancer, injected with ICG, and compare the imaging performance of the NIR-I window with that of the NIR-II window in each patient, to evaluate the potential of intraoperative NIR-II fluorescence imaging and NIR-II image-guided surgery in the clinic (Fig. 1).

Results

Integrated visible and NIR-I/II multispectral imaging instrument for clinical use. To translate the NIR-II imaging approach into the clinic, and understand its advantages and limitations over NIR-I imaging, we constructed an integrated visible and NIR-I/

¹CAS Key Laboratory of Molecular Imaging, Beijing Key Laboratory of Molecular Imaging, The State Key Laboratory of Management and Control for Complex Systems, Institute of Automation, Chinese Academy of Sciences, Beijing, China. ²University of Chinese Academy of Sciences, Beijing, China.

³Department of Hepatobiliary Surgery, Pathology and Nuclear Medicine, The Affiliated Hospital of Southwest Medical University, Luzhou, China.

⁴Engineering Research Center of Molecular and Neuro Imaging of Ministry of Education, School of Life Science and Technology, Xidian University, Xi'an, China. ⁵Molecular Imaging Program at Stanford, Bio-X Program, and Department of Radiology, Canary Center at Stanford for Cancer Early Detection, Stanford University, Stanford, CA, USA. ⁶Beijing Advanced Innovation Center for Big Data-Based Precision Medicine, School of Medicine, Beihang University, Beijing, China. ⁷These authors contributed equally: Zhenhua Hu, Cheng Fang, Bo Li, Zeyu Zhang. *e-mail: sgambhir@stanford.edu;

zcheng@stanford.edu; tian@ieee.org

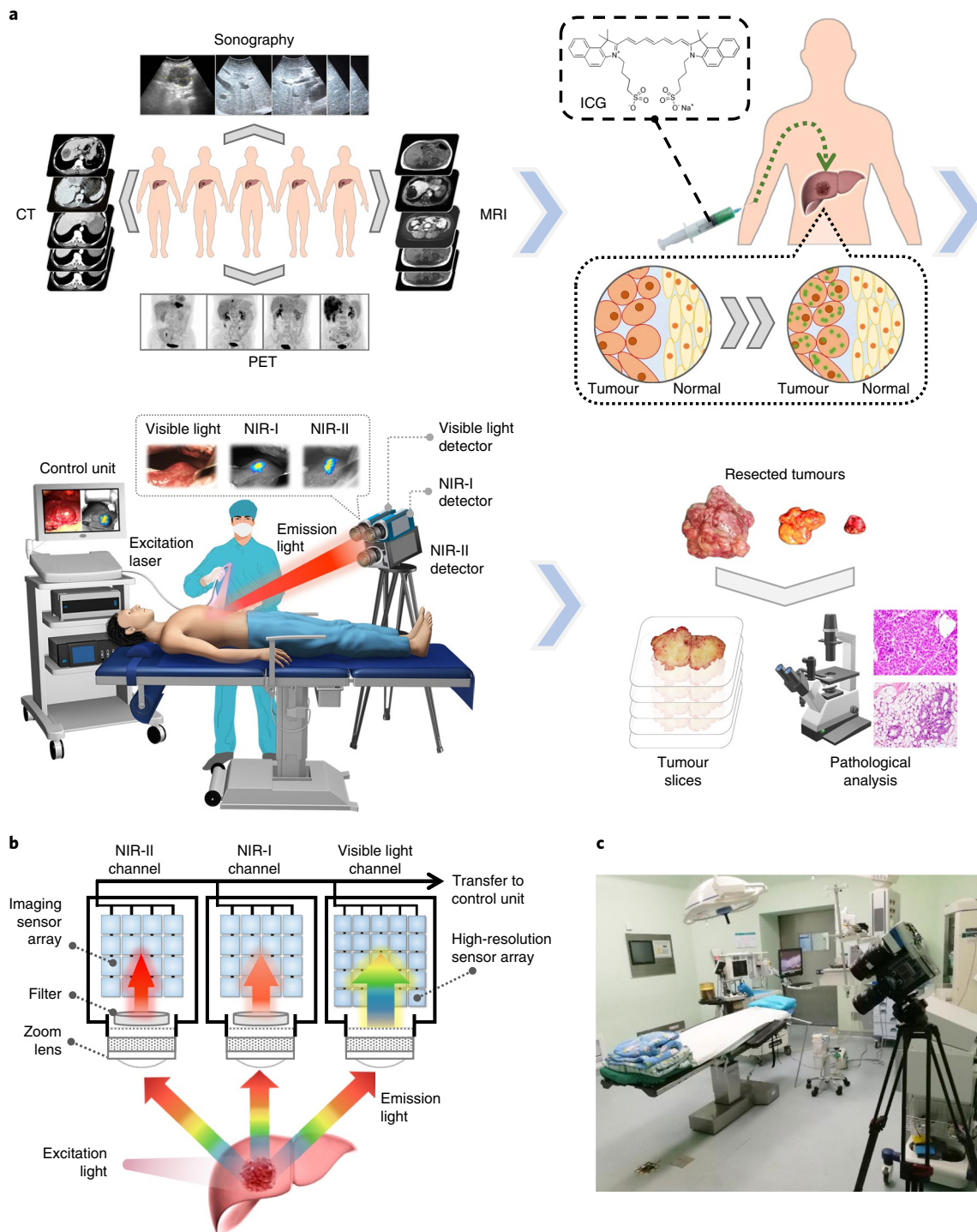


Fig. 1 | Description of the study plan and the visible and NIR-I/II multispectral imaging instrument for clinical applications. a, Patients with liver cancer were enrolled in the study, and then received preoperative imaging examinations, including enhanced CT, MRI, ultrasonography and PET. Before surgery, the patients were injected with ICG intravenously at a dose of 0.5 mg kg^{-1} body weight as a routine preoperative liver function test. One to seven days later, on the day of surgery, the patients received a laparotomy. The liver surface was examined by the integrated NIR-I/II and visible multispectral imaging instrument and visible and NIR-I/II images were obtained. Tumours were resected by the guidance of ultrasonography and NIR-I imaging. During the resection, NIR-II images were also acquired. After the operation, visible and NIR-I/II images of the resected specimens were obtained. Pathological examination of the resected tissues was conducted. **b**, Schematic of the integrated visible and NIR-I/II multispectral imaging instrument. **c**, The customized visible and NIR-I/II multispectral imaging instrument placed in the operating room.

II multispectral imaging instrument, covering the light spectrum range of 400–1,700 nm. This optical-imaging instrument consists of two sets of laser excitation equipment and three subsystems:

NIR-II imaging, NIR-I imaging and visible light imaging for acquiring NIR-II fluorescence, NIR-I fluorescence and tissue anatomical information, respectively (Fig. 1b). The specific parameters of this

instrument are listed in Supplementary Table 1. The multispectral instrument was easily placed in the surgical room for clinical use (Fig. 1c). Using the multispectral instrument, NIR-II and NIR-I imaging were performed in the operating room with illumination on and off, respectively (Supplementary Fig. 2a, NIR-II imaging; Supplementary Fig. 2b, NIR-I imaging).

NIR-I/II imaging of phantoms and tumour mice, and image-guided tumour resection. To further study the performance of the developed imaging instrument, phantoms and tumour-bearing mice were used, and image-guided tumour resection in animal models was performed. In the phantom imaging study, both the NIR-II and NIR-I fluorescence signal intensities linearly correlated with the increasing concentration of ICG in fetal bovine serum (FBS) (Supplementary Information and Supplementary Fig. 1a,b). Specifically, the correlation between NIR-I imaging intensity and ICG concentration was found to be $Y=0.73 \times X+0.69$ ($R^2=0.94$) for ICG in FBS (Supplementary Fig. 1b, left). Similarly, the correlation between NIR-II imaging intensity and ICG concentration was found to be $Y=0.45 \times X+0.19$ ($R^2=0.96$) for ICG in FBS (Supplementary Fig. 1b, right). Further quantitative analysis of the signal-to-background ratio (SBR) indicated that NIR-II imaging with ICG in FBS had a greater SBR, followed by NIR-I imaging with ICG in FBS (Supplementary Fig. 1c). For $4.5 \times 10^{-3} \text{ mg ml}^{-1}$ ICG, the SBR for NIR-II imaging and NIR-I imaging was 35.56 ± 0.26 and 16.85 ± 0.27 , respectively. The minimum detectable concentration of ICG by the instrument was 77.4 fM for NIR-II imaging and 6.45 fM for NIR-I imaging, indicating the high sensitivity of the multispectral imaging instrument.

Moreover, both NIR-I and NIR-II imaging clearly differentiated three phantoms (prepared with ICG dissolved in FBS in capillary glass tubes) (Fig. 2a, first row). When these samples were covered by chicken breast tissue with a thickness of 2.0 mm, the phantoms remained clearly imaged and discriminated (Fig. 2a, second row). However, when 5.0 mm of chicken breast tissue was used, NIR-I imaging failed to distinguish the three phantoms, whereas NIR-II imaging was still capable of differentiating the three sources (Fig. 2a, third row), demonstrating the higher optical resolution of NIR-II over NIR-I. Lastly, both NIR-I and NIR-II detected signals from the phantoms, but NIR-I imaging failed to differentiate them, and NIR-II imaging was still capable of differentiating the three sources when 8 mm of chicken breast tissue was used as a cover (Fig. 2a, fourth row). Further quantitative analysis showed that the fluorescence signal intensity and SBRs obtained from NIR-I and NIR-II decreased with increasing depth of the phantoms (Fig. 2b,c). But regardless of the phantom depth, the SBRs of NIR-II were always significantly higher than those of NIR-I ($P < 0.01$) (Fig. 2c), indicating that better imaging quality was achieved by NIR-II over NIR-I using the multispectral imaging instrument.

NIR-I and NIR-II imaging of subcutaneous HepG2 tumour-bearing mice ($n=3$ biologically independent animals per group) with tail-vein-injected ICG were further performed at 24 h post-injection. Both NIR-I and NIR-II imaging showed that ICG accumulated

in the tumour and liver with good contrast (Fig. 2d). Tumours were then removed in both groups of mice under the guidance of fluorescence imaging. Quantitative analysis showed that both the NIR-I and NIR-II signal from the tumour region and tumour-to-normal-tissue ratio (TNR) markedly dropped after the resection (Fig. 2e,f). Quantitative analysis indicated that preoperative NIR-II imaging showed a significantly higher TNR than that of NIR-I (2.25 ± 0.06 versus 1.48 ± 0.04 , $P < 0.001$), whereas postoperative NIR-II imaging showed a similar TNR to that of NIR-I (1.01 ± 0.02 versus 1.05 ± 0.04 , $P = 0.24$) (Fig. 2f). Moreover, the SBR for liver (defined as the liver-signal-to-skin ratio) obtained from preoperative and postoperative NIR-II imaging were also significantly higher than those obtained from the corresponding NIR-I imaging ($P < 0.01$).

Intraoperative NIR-I/II imaging of patients with primary hepatocellular carcinoma, intrahepatic metastasis or extrahepatic metastasis. Patients with liver cancer ($n=23$) were enrolled in the group (details of patient characteristics are listed in Supplementary Table 2), and they received preoperative imaging examinations, including enhanced computed tomography (CT), magnetic resonance imaging (MRI), ultrasonography and positron emission tomography (PET). Before surgery, the patients were injected with ICG intravenously at a dose of 0.5 mg kg^{-1} body weight as a routine preoperative liver function test. One to seven days later, on the day of surgery, the patients received a laparotomy. The liver surface was examined by the multispectral imaging instrument and visible, NIR-I and NIR-II images were obtained. Tumours were surgically resected by the guidance of intraoperative in vivo ultrasonography and NIR-I imaging, while in vivo NIR-II imaging was performed as a contrast. The resected tumours were also imaged with intraoperative ex vivo visible, NIR-I and NIR-II imaging.

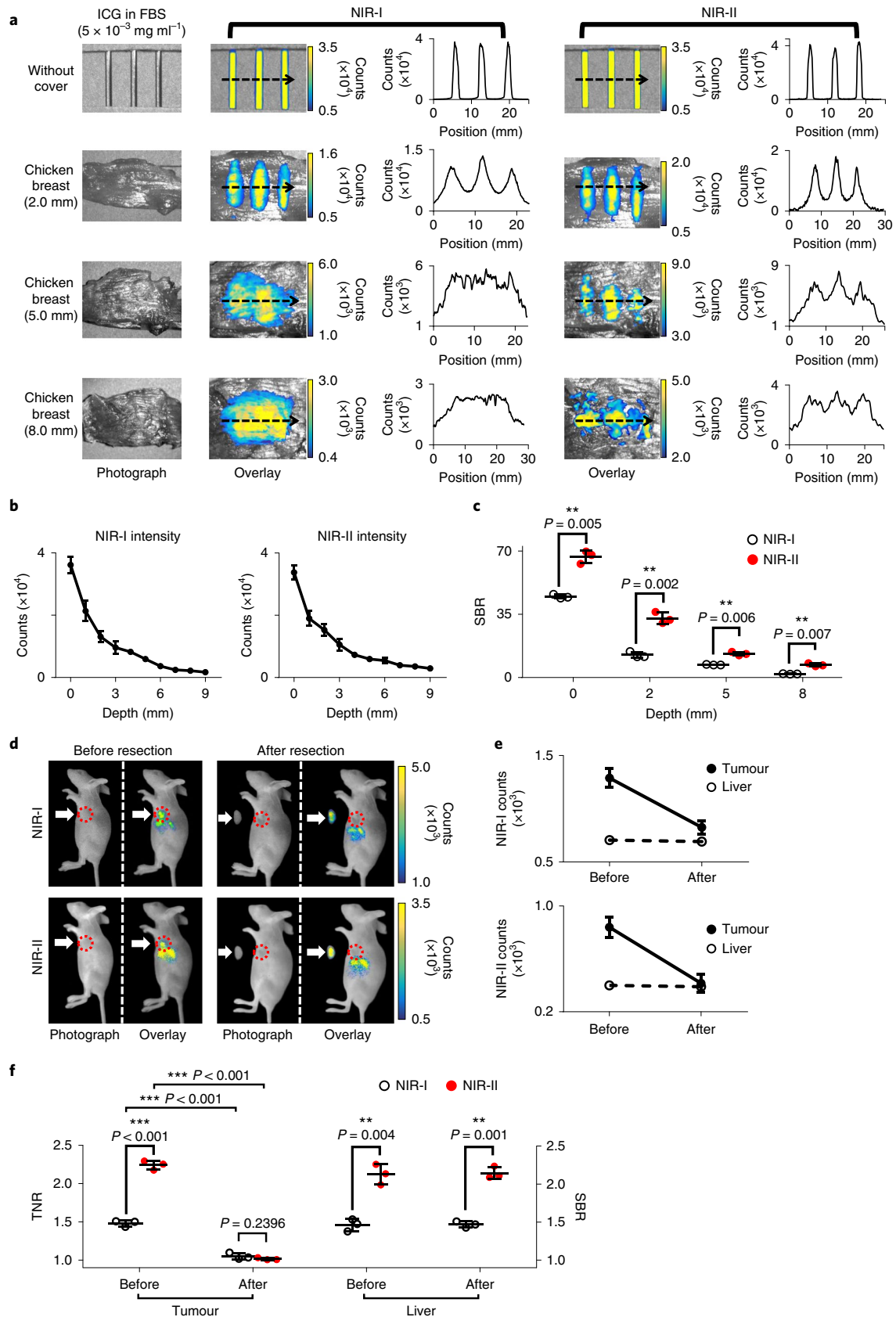
The effects on image quality from environmental light were briefly tested. For a typical patient with liver cancer, the tumour could be identified in the visible light image using the multispectral instrument, as indicated by the white arrows in Supplementary Fig. 2c. We found that NIR-II imaging was barely affected by the illumination of operating room (Supplementary Fig. 2d). In contrast, NIR-I fluorescence was strongly disturbed and unable to be differentiated under room illumination (Supplementary Fig. 2e). In another patient, visible and NIR-II images of the liver surface were efficiently acquired with room illumination on (Supplementary Fig. 2f,g), whereas illumination off was necessary to acquire clear NIR-I tumour images (Supplementary Fig. 2h). Hence, in the following experiments, NIR-I imaging was always performed with room illumination off in this study.

For a typical patient with hepatocellular carcinoma (HCC), preoperative enhanced CT showed a tumour located in liver segments VII and VIII (Couinaud segmentation) (Fig. 3a). The liver surface was visualized by visible light imaging (Fig. 3b). A nodule of liver cancer was successfully detected by an intense NIR-II and NIR-I fluorescence signal using intraoperative NIR-II and NIR-I imaging (Fig. 3c,d and Supplementary Fig. 8b,c). For a typical patient with intrahepatic metastasis, enhanced CT images showed two meta-

Fig. 2 | Comparison of the penetration and resolution of NIR-II and NIR-I imaging and the NIR-I/II image-guided tumour resection of subcutaneous HepG2 tumour-bearing mice. **a**, Visible light images and NIR-I/II images of the capillary glass tubes containing ICG dissolved in FBS. Arrows correspond to the location and direction of cross-sectional fluorescence intensity profiles for both the NIR-I and NIR-II regions. The capillary glass tubes were covered by chicken breast tissue with various thickness (1.0, 2.0, 3.0, 4.0, 5.0, 6.0, 7.0, 8.0 and 9.0 mm). **b**, The NIR-I/II fluorescence signal intensity decreased with increasing depth of the capillary glass tubes. **c**, There was a significant difference between the SBR of NIR-II and NIR-I imaging at various depths ($P < 0.01$). Significance was calculated by a two-sided Welch's *t*-test. $**P < 0.01$. **d**, The detection of the subcutaneous HepG2 tumour and image-guided resection by NIR-I/II imaging (first row and second row, resection guided by NIR-I and II imaging, respectively.). **e**, The NIR-I/II signal in the tumour position dropped dramatically after resection. **f**, Quantitative analysis indicated that preoperative NIR-II imaging showed a significantly higher TNR than that of NIR-I (2.25 ± 0.06 versus 1.48 ± 0.04 , $P < 0.001$), whereas postoperative NIR-II imaging showed a slightly lower TNR than that of NIR-I but with no significant difference (1.01 ± 0.02 versus 1.05 ± 0.04 , $P = 0.2396$). Significance was calculated by a two-sided Welch's *t*-test. $**P < 0.01$; $***P < 0.001$. Data in **b**, **c**, **e** and **f** are mean \pm s.d.

static lesions in the liver (as one representative lesion, indicated by the red arrow in Fig. 3e). The multispectral instrument also detected the two intrahepatic metastases (Fig. 3f–h and Supplementary Fig.

8d–f) and visualized them, individually. For a typical patient with extrahepatic metastasis, both preoperative CT and PET imaging indicated primary liver cancer in liver segments II and III, but failed



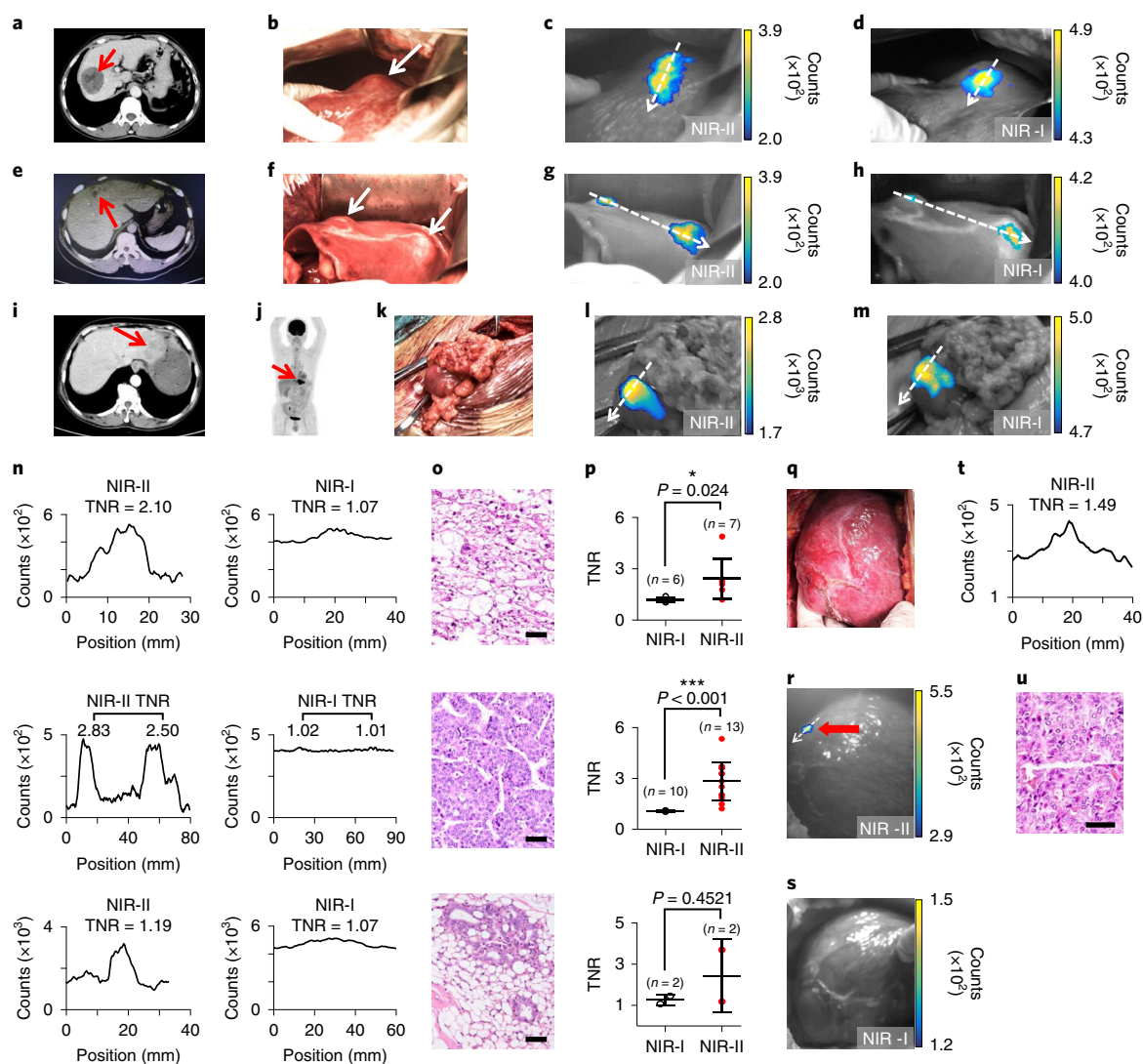


Fig. 3 | Intraoperative NIR-II/I imaging of patients with primary HCC, intrahepatic metastasis or extrahepatic metastasis. A total of 1,057 intraoperative fluorescence images, including 490 NIR-I images and 567 NIR-II images, were obtained. Additional results are included in Supplementary Figs. 2–8. **a**, For a typical patient with HCC, preoperative enhanced CT showed a tumour located in liver segments VII and VIII. **b**, The liver surface was visualized by visible light imaging with illumination from sunlight lamps in the surgery room. **c,d**, A nodule of liver cancer was successfully detected as intense NIR-II (**c**) and NIR-I (**d**) fluorescence signals using intraoperative NIR-II and NIR-I imaging. **e**, For a typical patient with intrahepatic metastasis, enhanced CT images showed two metastatic lesions in the liver (as one representative lesion indicated by the red arrow). **f–h**, The multispectral instrument detected two intrahepatic metastases, showing them separately, using visible light imaging (**f**), and intraoperative NIR-II (**g**) and NIR-I (**h**) imaging. **i–m**, For a typical patient with extrahepatic metastasis, preoperative CT (**i**) and PET (**j**) images clearly showed primary liver cancer in liver segments II and III and there was no extrahepatic metastasis. However, after the laparotomy, intraoperative NIR-II (**l**) and NIR-I (**m**) imaging found the metastatic lesion in the omentum (**k**). **n**, White arrows correspond to the location and the direction of cross-sectional fluorescence intensity profiles for both the NIR-II and NIR-I regions. The quantitative analysis results also showed that the NIR-II imaging discriminated a nodule of liver cancer more effectively compared with NIR-I. **o**, The H&E results showed that the tumours were well-differentiated HCC (top), moderately differentiated HCC (middle) and ICC (bottom). Scale bar, 50 μm . **p**, For all the patients with primary HCC ($n=11$), NIR-II imaging achieved a significantly higher TNR over NIR-I imaging ($P=0.024$, top). For all the patients with intrahepatic metastasis ($n=9$), intraoperative NIR-II imaging showed a significantly higher TNR over NIR-I imaging ($P<0.001$, middle). Lastly, it was found that the TNRs of NIR-II imaging obtained from two patients with extrahepatic metastasis were higher than those of NIR-I (bottom). Each point in the figure represents the result from one patient. Data are mean \pm s.d. Significance was calculated by a two-sided Welch's *t*-test. $*P<0.05$; $***P<0.001$. **q**, For a typical patient with HCC, the liver surface was visualized by visible light imaging. **r**, A small intrahepatic metastasis in the right liver was successfully detected by NIR-II imaging, as shown by the red arrow. **s**, However, NIR-I imaging failed to detect the lesion. **t**, The TNR of NIR-II was 1.49. **u**, Histopathological examination using H&E staining showed that the dissected lesion was moderately differentiated HCC. Scale bar, 50 μm .

to detect the extrahepatic metastasis (Fig. 3i,j). After laparotomy, intraoperative NIR-II and NIR-I imaging revealed the metastatic lesion in the omentum (Fig. 3k–m and Supplementary Fig. 8g–i) and the peritoneum (data not shown). These results demonstrated that the combination of intraoperative NIR-II and NIR-I fluorescence

imaging detected extrahepatic metastases overlooked by preoperative modalities, and that this finding changed the patient's staging and treatment options.

In these three representative examples, the white arrows correspond to the location and direction of cross-sectional fluorescence

intensity profiles for both the NIR-II and NIR-I regions. The quantitative analysis results also showed that the NIR-II imaging discriminated a nodule of liver cancer more effectively compared with NIR-I (Fig. 3n). All the TNRs of NIR-II were much higher than those of NIR-I (primary HCC, 2.10 versus 1.07; intrahepatic metastasis, 2.83 versus 1.02 and 2.50 versus 1.01; extrahepatic metastasis, 1.19 versus 1.07). Further histopathological examination using hematoxylin and eosin (H&E) staining demonstrated that the dissected tumours were well-differentiated HCC (Fig. 3o, top), moderately differentiated HCC (Fig. 3o, middle) and moderately differentiated cholangiocellular carcinoma (ICC) (Fig. 3o, bottom).

In this study, for all the patients with solitary HCC ($n = 11$), intraoperative NIR-II imaging detected seven HCC nodules, including two well-differentiated HCCs and five moderately differentiated HCCs. Intraoperative NIR-I imaging detected six HCC nodules, including two well-differentiated HCCs and four moderately differentiated HCCs. NIR-II imaging achieved a much higher TNR over NIR-I imaging (Fig. 3p, top; 2.43 ± 1.16 versus 1.17 ± 0.13 , $P = 0.024$). For all the patients with intrahepatic metastasis ($n = 9$), intraoperative NIR-II imaging detected nine primary HCCs and four intrahepatic metastases, whereas NIR-I imaging detected seven primary HCCs and three intrahepatic metastases. Intraoperative NIR-II imaging also showed a much higher TNR over NIR-I imaging for these patients (Fig. 3p, middle; 2.83 ± 1.13 versus 1.07 ± 0.04 , $P < 0.001$). Lastly, it was found that the TNRs of NIR-II imaging obtained from two patients with extrahepatic metastasis were higher than those of NIR-I (Fig. 3p, bottom).

We also found that NIR-II imaging was able to visualize some tumour lesions that were missed by NIR-I imaging. For example, the liver surface was visualized by visible light imaging in a patient with HCC (Fig. 3q). A small intrahepatic metastasis in the right liver was successfully detected by NIR-II imaging, as shown by the red arrow in Fig. 3r. However, NIR-I imaging failed to detect the lesion (Fig. 3s). The TNR of NIR-II was 1.49 (Fig. 3t). Histopathological examination using H&E staining showed that the dissected lesion was moderately differentiated HCC (Fig. 3u).

Intraoperative fluorescence image-guided tumour resection. Tumour lesions recognized by surgeons first received visible light imaging by the multispectral imaging instrument (Fig. 4a). NIR-II fluorescence also identified the location of the tumour (Fig. 4b). The NIR-I fluorescence distribution pattern was consistent with that of the NIR-II image (Fig. 4c). Guided by ultrasonography and the visible light image, the tumour was resected and thought to be completely removed on the basis of the experience of the surgeons (Fig. 4d). Intraoperative ultrasonography also verified that there was no residual tumour (Fig. 4j). However, NIR-II and NIR-I imaging still detected fluorescence from the remaining tissue (Fig. 4e,f). Then, on the basis of the NIR-I images, further resection was performed. After this second resection, visual inspection indicated that

there was no residual tumour (Fig. 4g), and optical imaging showed no NIR-II or NIR-I fluorescence in the remaining tissue either (Fig. 4h,i). The abovementioned two resected tissues were imaged and are shown in Fig. 4k,l, respectively. Quantitative analysis indicated that both the NIR-I and NIR-II signals from the tumour region had no obvious change after the first resection but hugely dropped after the second resection (Fig. 4m). For the first resection, the TNR of NIR-II imaging was also higher than that of NIR-I, and there was no difference for the TNR of NIR-II and NIR-I after the second resection (Fig. 4n). H&E staining showed that the two resected tumour tissues were both HCC (Fig. 4o). The results indicated that both intraoperative NIR-I and NIR-II imaging detected residual HCC, which were undetected by visual inspection and intraoperative ultrasonography.

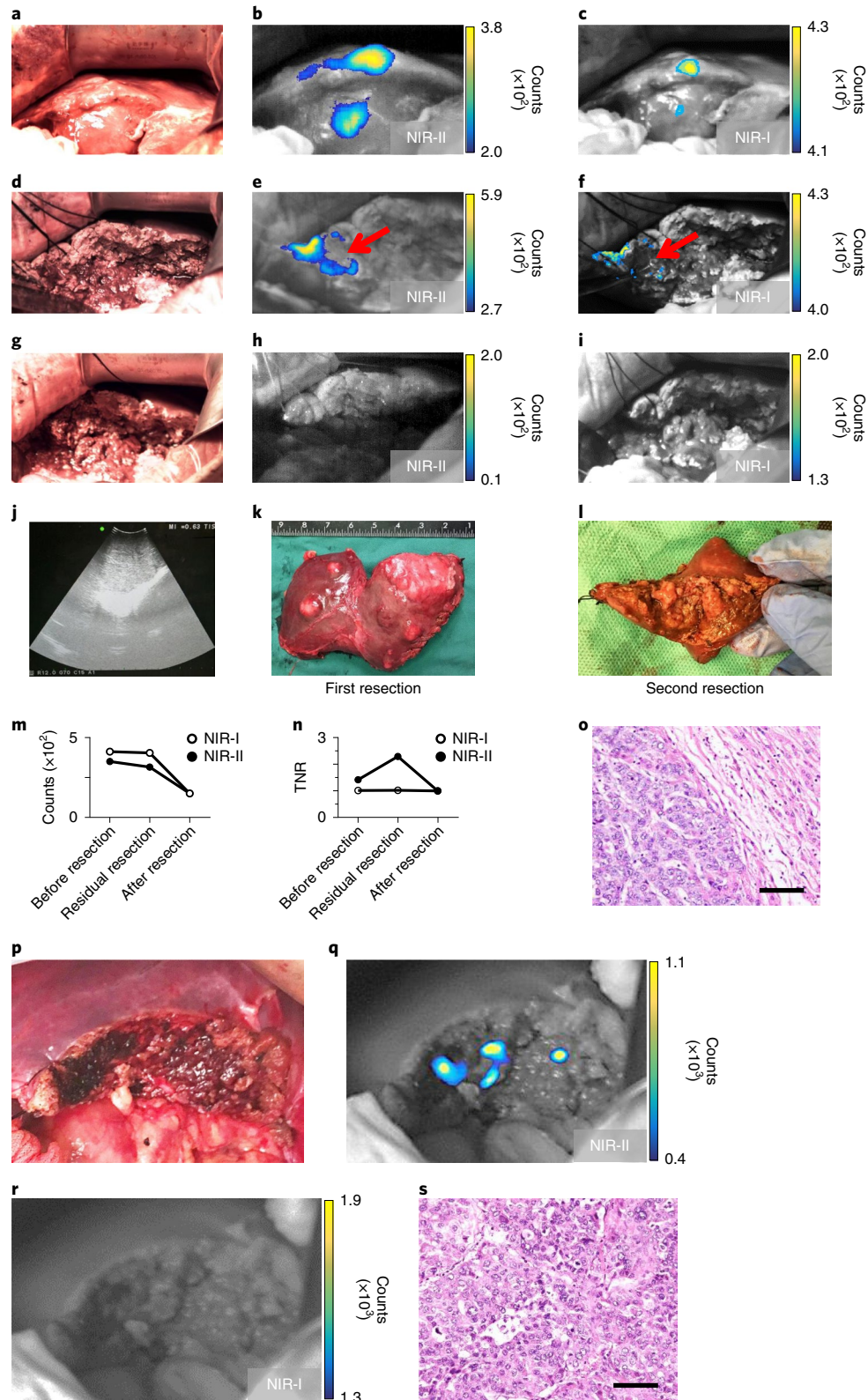
NIR-II imaging also demonstrated the capability to delineate lesions that were missed by NIR-I imaging in the image-guided resection procedure. For a typical patient with HCC, guided by ultrasonography and the visible light image, the tumour was resected and considered to be completely removed on the basis of the experience of the surgeons (Fig. 4p). However, NIR-II imaging detected a residual fluorescent lesion (Fig. 4q) and NIR-I imaging failed to reveal any signals (Fig. 4r). This fluorescent lesion was confirmed as abnormal by surgeons and then resected. Postoperative histopathological examination proved that the resected abnormal tissue was HCC (Fig. 4s).

NIR-I/II imaging of the resected specimens. A typical primary HCC was resected and then clearly delineated ex vivo from intraoperative visible light, NIR-II and NIR-I images (Supplementary Fig. 3a–c). For a representative intrahepatic metastasis, the resected tumour specimen was sliced and imaged intraoperatively with the multispectral imaging instrument (Supplementary Fig. 3d–i). NIR-II and NIR-I imaging identified three extra lesions that were undetected by preoperative CT, as indicated by white and red arrows in Supplementary Fig. 3e–i. For an extrahepatic metastasis, on the basis of the NIR-I image, the metastatic lesion was resected (Supplementary Fig. 3j), and NIR-II and NIR-I fluorescence was observed from the resected tumour specimen (Supplementary Fig. 3k,l). The quantitative analysis showed that the NIR-II imaging discriminated lesions more effectively compared with NIR-I (Supplementary Fig. 3m–o). All the TNRs of NIR-II were much higher than those of NIR-I (primary HCC, 1.37 versus 1.04; intrahepatic metastasis, 2.63 versus 1.11 and 2.00 versus 1.24; extrahepatic metastasis, 5.73 versus 1.15). The H&E results demonstrated that the primary tumour was well-differentiated HCC (Supplementary Fig. 3p). For the intrahepatic metastases, one was found to be focal nodular hyperplasia (Supplementary Fig. 3q, number 1) and the other two were shown to be HCC (Supplementary Fig. 3r,s, numbers 2 and 3). The extrahepatic metastasis was shown to be HCC (Supplementary Fig. 3t).

Fig. 4 | Intraoperative NIR-I/II fluorescence image-guided tumour resection. **a**, For a typical NIR-I image-guided surgery study, the visible image first showed a lesion in the liver tissue. **b**, NIR-II fluorescence also identified the location of the tumour. **c**, The NIR-I fluorescence distribution pattern was consistent with that of the NIR-II imaging. **d**, Guided by ultrasonography and the visible light image, the tumour was resected and thought to be completely removed on the basis of the experience of the surgeons. **j**, Intraoperative ultrasonography also verified there was no residual tumour. **e,f**, However, NIR-II (**e**) and NIR-I (**f**) imaging still detected fluorescence in the residual tissue (indicated by red arrows). Then, on the basis of the NIR-I image, further resection was performed. **g**, After this second resection, visual inspection indicated there was no residual tumour. **h,i**, Further, there was no NIR-II (**h**) or NIR-I (**i**) fluorescence signal in the residual tissue. **k,l**, The first (**k**) and second (**l**) resected tissues. **m**, Quantitative analysis indicated that both the NIR-I and NIR-II signals from the tumour region had no obvious change after the first resection, but hugely dropped after the second resection. **n**, For the first resection, the TNR of NIR-II imaging was also higher than that of NIR-I, and there was no difference for the TNR of NIR-II and NIR-I after the second resection. **o**, The two resected tumour tissues were shown to be HCC. Scale bar, 50 μm . **p**, For a typical patient with HCC, guided by ultrasonography and the visible light image, the tumour was resected and thought to be completely removed on the basis of the experience of the surgeons. **q**, NIR-II imaging detected fluorescence signals in the remaining tissue sections. **r**, NIR-I imaging did not reveal any signals. **s**, The fluorescent residual tissues were further resected and received histopathological examination to verify that the tissues were HCC. Representative H&E staining image showed that the resected lesion was HCC. Scale bar, 50 μm .

For a typical patient with HCC (Fig. 3a–d), intraoperative NIR-II and NIR-I imaging detected the lesion (Fig. 3c,d). The intraoperative ultrasonography was used for demonstrating the position, depth and size of the tumour (Supplementary Fig. 4a). The resected fluorescent tissue (Supplementary Fig. 4b) was transversely incised into two parts along the maximum tumour diameter (Supplementary Fig.

4c). NIR-II and NIR-I fluorescence imaging was performed on the tumour specimen and no fluorescence was acquired in the normal liver tissues (Supplementary Fig. 4d, visible image; Supplementary Fig. 4e, NIR-II; Supplementary Fig. 4f, NIR-I). The quantitative analysis results showed that the NIR-II imaging discriminated lesions more effectively compared with NIR-I (Supplementary Fig. 4g,h).



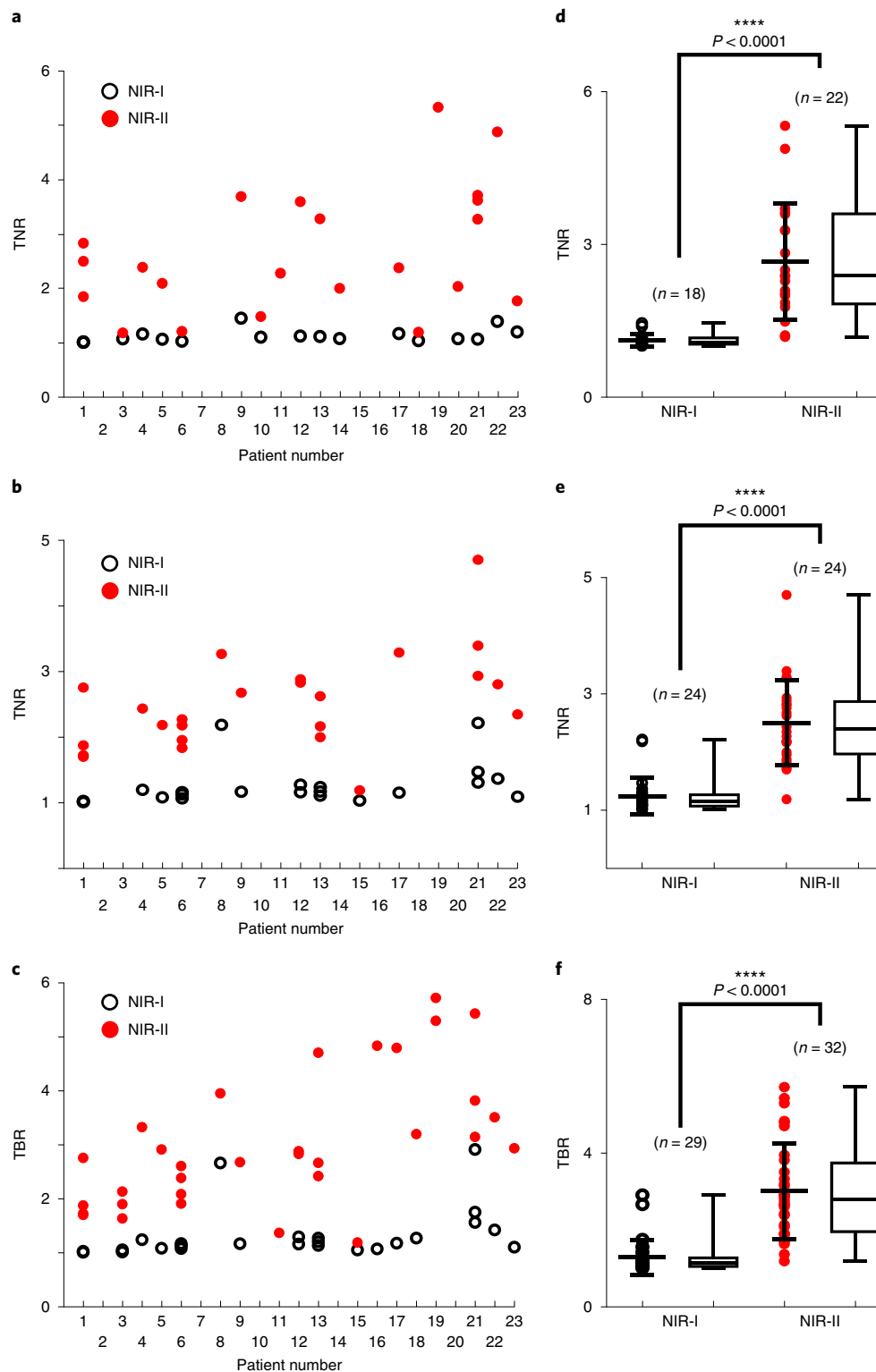


Fig. 5 | Comparison of TNR or TBR for NIR-II and NIR-I imaging. **a**, Quantitative analysis of the TNR of NIR-II and NIR-I imaging in the in vivo experiment. **b**, Quantification analysis of the TNR of NIR-II and NIR-I imaging in the ex vivo experiment. **c**, Quantitative analysis of the TBR of NIR-II and NIR-I imaging in the ex vivo experiment. Quantitative analysis of all patients clearly showed that the TNR or TBR for NIR-II imaging was much larger than that for NIR-I imaging both in the in vivo and ex vivo experiments. NIR-II, red solid circle; NIR-I, black hollow circle. **d**, In the in vivo experiment, there was a significant correlation difference between the TNR of NIR-II and NIR-I ($P < 0.0001$). The TNR of the NIR-II imaging results was obviously higher than that of the NIR-I results. **e**, In the ex vivo experiments, the TNR of NIR-II imaging was significantly higher than that of NIR-I imaging ($P < 0.0001$). **f**, In the ex vivo experiments, the TBR of NIR-II imaging was superior compared with NIR-I imaging ($P < 0.0001$). Data in **d-f** are mean \pm s.d. Data range, median and quartiles are shown as box plots in **d-f**. Significance was calculated by a two-sided Welch's *t*-test. **** $P < 0.0001$.

For another typical patient with HCC (Supplementary Fig. 4i), intraoperative fluorescence imaging did not detect any lesions; however, the intraoperative ultrasonography detected a tumour at a depth of 20 mm (Supplementary Fig. 4j). The tumour was resected (Supplementary Fig. 4k). The specimen was transversely incised to expose the maximum tumour section, and was further sliced into pieces of approximately 10 mm thickness (Supplementary Fig. 4l). Every section received fluorescence imaging to detect all the tumour lesions. The NIR-II and NIR-I imaging results showed the cirrhotic nodule had no NIR-II or NIR-I fluorescence, while the tumour tissues were fluorescent (Supplementary Fig. 4m, visible image; Supplementary Fig. 4n, NIR-II; Supplementary Fig. 4o, NIR-I). The H&E results confirmed that the tissue with the strongest optical signal (Supplementary Fig. 4m, arrow 1) was solid-type HCC (Supplementary Fig. 4p), the tissue with relatively weak fluorescence (Supplementary Fig. 4m, arrow 2) was glandular-type HCC (Supplementary Fig. 4q) and the non-fluorescent tissue (Supplementary Fig. 4m, arrow 3) was a cirrhotic nodule (Supplementary Fig. 4r). The quantitative analysis demonstrated again that NIR-II imaging had a stronger performance than NIR-I imaging in tumour identification (Supplementary Fig. 4s,t).

Comparison of imaging contrast ratio between NIR-I and NIR-II imaging. The fluorescence intensity of tumour, normal liver tissue and ex vivo imaging background were plotted (Supplementary Fig. 9). The quantified data are listed in Supplementary Table 3. Tumour tissue, normal tissue or background could be differentiated by NIR-I or NIR-II fluorescence intensity. Notably, the differences between tumour signals and normal-tissue signals or background in NIR-II imaging were much more pronounced than those from NIR-I imaging, explaining why NIR-II imaging had improved performance in identifying lesions compared with NIR-I.

Quantitative analysis of all patients clearly showed that the TNR or tumour-to-background ratio (TBR) of NIR-II imaging was much higher than that of NIR-I imaging both in the in vivo and ex vivo imaging studies (Fig. 5a–c). The TNRs and TBRs of the NIR-I/II imaging studies are listed in Supplementary Table 6. In the in vivo imaging study, the mean TNR of NIR-II imaging was 2.66 ± 1.14 , which was almost 2.4-fold higher than that of NIR-I (1.12 ± 0.12). The maximum TNR of in vivo NIR-II imaging and TBR of ex vivo NIR-II imaging were 5.33 and 5.72, respectively. However, the maximum TNR of in vivo NIR-I imaging and TBR of ex vivo NIR-I imaging were only 1.45 and 2.92, respectively. For both in vivo and ex vivo imaging studies, there was a significant improvement of the imaging contrast ratio in NIR-II compared with NIR-I (Fig. 5d–f; $P < 0.0001$ for in vivo and ex vivo). The distribution of the TNR/TBR for NIR-II imaging was found to be mainly in the range of 2–4, much higher than that for NIR-I, which was mainly in the range of 1–2 (Fig. 5d–f).

Comparison of malignant tumour-detection ability of NIR-I and NIR-II imaging. Overall, 23 patients had a total of 39 lesions including the primary tumour and metastases. Preoperative imaging modalities identified 34 malignant lesions. NIR-II imaging detected 35 malignant lesions and NIR-I identified 32 malignant lesions. The results are listed in Supplementary Table 7. NIR-II imaging identified 30 of 34 preoperatively diagnosed malignant lesions, including 20 lesions visualized by intraoperative in vivo NIR-II fluorescence imaging and the other 10 found in the sectioned specimens by intraoperative ex vivo NIR-II imaging. There were four lesions not detected by NIR-II imaging. However, other than preoperatively diagnosed lesions, NIR-II fluorescence imaging visualized five additional malignant lesions, including two detected by intraoperative in vivo NIR-II imaging and three found in NIR-II imaging of specimens (Fig. 6a).

NIR-I imaging identified 27 of 34 preoperatively diagnosed malignant lesions, including 17 lesions visualized by intraopera-

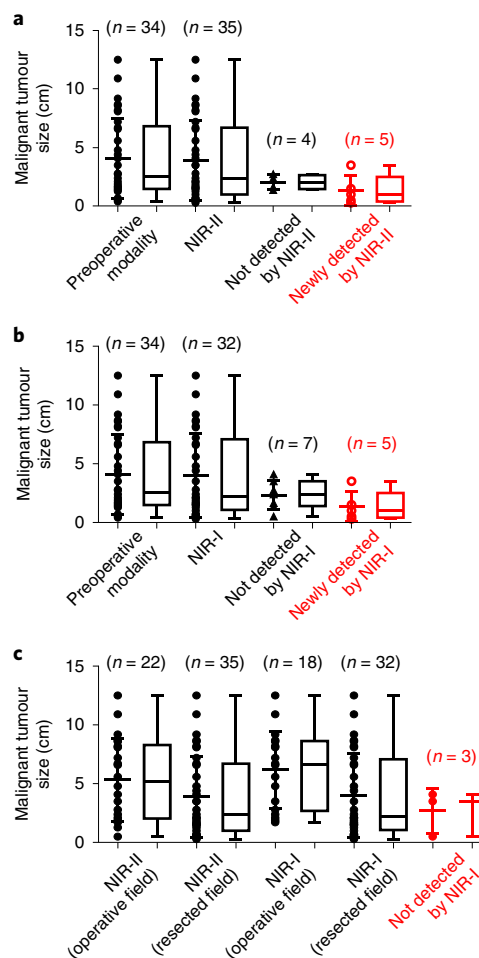


Fig. 6 | Comparison of tumour-detection ability of NIR-I/II imaging.

a, Preoperative imaging modalities identified 34 lesions. A total 35 lesions were found by NIR-II imaging. NIR-II imaging identified 30 of 34 preoperatively diagnosed lesions. There were 4 of these 34 lesions that were not detected by NIR-II imaging. However, other than preoperatively diagnosed lesions, NIR-II fluorescence imaging visualized six new lesions. Five lesions were malignant and one was benign. **b**, NIR-I imaging detected a total of 32 lesions. NIR-I imaging identified 27 of 34 preoperatively diagnosed lesions. There were seven lesions that were not detected by NIR-I imaging. Besides the preoperatively diagnosed lesions, NIR-I fluorescence imaging also visualized six new lesions (five malignant lesions and one benign lesion). **c**, A total of 35 tumours were found by NIR-II imaging, including the in vivo intraoperative imaging and the ex vivo resected specimen imaging. Intraoperative NIR-II imaging visualized 22 lesions. The other 13 lesions were found in the sectioned specimens by NIR-II imaging. NIR-I imaging detected a total of 32 tumours: 18 tumours were detected in the intraoperative imaging and 14 tumours were detected in the resected specimen imaging. The 32 lesions detected by NIR-I imaging were all detected by NIR-II imaging. It is worth noting that NIR-II imaging found three extra tumours that could not be found by NIR-I imaging. Data range, median and quartiles are shown as box plots in **a–c**.

tive in vivo NIR-I fluorescence imaging and the other 10 found by intraoperative ex vivo NIR-I imaging. There were seven lesions not detected by NIR-I imaging. However, other than preoperatively diagnosed lesions, NIR-I fluorescence imaging also visualized five additional malignant lesions, including one detected by intraoperative in vivo NIR-I imaging, and four found by ex vivo NIR-I imaging on specimens (Fig. 6b).

Table 1 | Diagnostic results of NIR-II and NIR-I imaging

		Gold standard Positive	Gold standard Negative	CI	Sensitivity (%)	Specificity (%)	PPV	NPV	Accuracy
NIR-II	Positive	32	3	95%	100	88.46	91.43	100	91.43
	Negative	0	23		89.1–100	69.85–97.55	76.9–98.2	85.18–100	76.9–98.2
NIR-I	Positive	29	3	95%	90.63	88.46	90.63	88.46	82.86
	Negative	3	23		75.0–98.0	69.85–97.55	75.0–98.0	69.85–97.55	66.4–93.4

PPV, positive predictive value; NPV, negative predictive value.

The six lesions newly detected by NIR-II or NIR-I imaging included three HCCs (three were moderately differentiated), two ICCs and one benign lesion (Supplementary Table 4). The benign lesion was later diagnosed as a focal nodular hyperplasia by histopathological analysis. Except one ICC, the diameter of the newly detected lesions was below 15 mm.

For the 35 tumours found by intraoperative NIR-II imaging, 22 tumours were visualized by *in vivo* imaging, and the other 13 tumours were found in the sectioned specimens by *ex vivo* imaging (Fig. 6c). Intraoperative NIR-I imaging detected 32 tumours in total: 18 tumours were detected *in vivo* and 14 tumours were detected in the resected specimen imaging. All of the 32 lesions detected by NIR-I imaging were also detected by NIR-II imaging. It is worth noting that NIR-II imaging found three extra tumours that were not detectable by NIR-I imaging.

The malignant tumour-detection rate of intraoperative *in vivo* NIR-II and NIR-I fluorescence imaging was calculated to be 56.41% (22/39, 95% confidence interval (CI) 39.6%–72.2%) and 46.15% (18/39, 95% CI 30.1%–62.8%), respectively. The detection rate was 100% (32/32, 95% CI 89.1%–100%) and 90.63% (29/32, 95% CI 75.0%–98.0%) for *ex vivo* NIR-II and NIR-I fluorescence imaging, respectively (Supplementary Table 5). Moreover, the detection sensitivity of NIR-II imaging was 100% (32/32, 95% CI 89.1%–100%) and its positive predictive value was 91.43% (32/35, 95% CI 76.9%–98.2%), while the sensitivity of NIR-I imaging was 90.63% (29/32, 95% CI 75.0%–98.0%) and its positive predictive value was 90.63% (29/32, 95% CI 75.0%–98.0%) (Table 1). Lastly, the accuracy of tumour detection of NIR-II and NIR-I imaging was calculated to be 91.43% (32/35, 95% CI 76.9%–98.2%) and 82.86% (29/35, 95% CI 66.4%–93.4%), respectively.

Discussion

Fluorescence detection in the NIR-II window provides many advantages over the more conventional NIR-I imaging, including improved imaging depth sensitivity, higher spatial resolution and imaging contrast in small-animal models^{15,16}, and thus represents a promising field of study. Considering the interest in pursuing clinical NIR-I imaging, demonstrated by recent literature on the topic, and the potential utility that the NIR-I spectral window has for disease diagnosis and image-guided surgery^{8–12}, it is both crucial and urgent to determine whether NIR-II imaging provides similar benefits in clinical scenarios, and to evaluate its performance compared with NIR-I imaging. We have thus developed an integrated visible and NIR-II/I multispectral imaging instrument and performed the first-in-human study testing NIR-II imaging in a group of patients with liver cancer. The results will help to understand the potential role of NIR-II imaging in patient diagnosis and management, and to determine the advantages and limitations of both NIR windows in human applications.

The optical-imaging instrument covers the whole spectrum of visible, NIR-I and NIR-II light, providing the capability to image diseased tissue using a wide range of optical probes detectable in the NIR-I/II windows, and to directly compare the imaging perfor-

mance of NIR-II and NIR-I in the same patients. An experiment carried out on a phantom containing ICG samples showed that the detection sensitivity of the multispectral instrument is 77.4 fM for NIR-II imaging and 6.45 fM for NIR-I imaging, suggesting that the instrument can detect targets with very low concentrations of contrast agent. It should also be noted that the higher sensitivity *in vitro* observed for ICG in the NIR-I over the NIR-II window is mainly attributed to the peak fluorescence emission intensity displayed by ICG in the NIR-I window, than in the tail-end of its emission in the NIR-II window.

Moreover, the phantom study shows that the optical resolution of NIR-II imaging is higher than that of NIR-I imaging. NIR-II imaging can distinguish three light sources underneath 8.0 mm of chicken breast tissue, whereas NIR-I imaging failed at this depth (Fig. 2a). Better imaging quality is also achieved using NIR-II imaging, compared with NIR-I, in small-animal models (Fig. 2d–f), mainly attributed to reduced tissue autofluorescence, reduced photon scattering and the low levels of photon absorption at longer wavelengths^{15,16}. These results highlight the improved imaging performance of NIR-II over NIR-I, which are also consistent with previous findings^{26,29–31}.

Both *in vivo* and *ex vivo* intraoperative tumour imaging in patients clearly demonstrate that NIR-II imaging shows better image quality than NIR-I (Figs. 3 and 4). The TNRs or TBRs of NIR-II fluorescence imaging are significantly higher than that of NIR-I fluorescence imaging. During intraoperative *in vivo* imaging, the TNR of NIR-II imaging reached as high as 5.33, whereas the maximum TNR for NIR-I imaging was only 1.45 (Fig. 5). In the *ex vivo* imaging study, the TBR of NIR-II imaging was 5.72, almost twice the TBR of NIR-I imaging (only 2.92). Consistent with the high imaging contrast obtained for intraoperative NIR-II imaging, it also shows a higher malignant tumour-detection rate than that of NIR-I (*in vivo* imaging: 56.41% versus 46.15%; *ex vivo* imaging of resected specimens: 100% versus 90.63%) (Supplementary Table 5). This result is in line with the rate of HCC detection using intraoperative NIR-I fluorescence imaging (52–100%) or postoperative NIR-I imaging of resected tissue (100%) reported in the literature^{33–36}. Moreover, the tumour-detection sensitivity of NIR-II and NIR-I imaging has been found to be 100% and 90.63%, and its positive predictive value is 91.43% and 90.63%, respectively (Table 1). Thus, NIR-II imaging shows a higher tumour-detection sensitivity and positive predictive value than that of NIR-I. All of these comparisons strongly suggest that NIR-II imaging is a better technique than NIR-I in clinical intraoperative liver-cancer imaging and image-guided surgery. A further advantage of using NIR-II imaging is its compliance with operating-room illumination, compared with NIR-I imaging that requires the lights to be switched off. This feature of NIR-II imaging provides convenience and feasibility for clinical applications. The advantages of complementing NIR-II and NIR-I for ICG detection during image-guided surgery of liver cancer are unclear. Further investigations of whether both windows can be combined to improve tumour imaging and treatment by using two or multiple probes specifically optimized for NIR-II and NIR-I

imaging will be needed. The integrated imaging system developed in this study provides a solid foundation for this research direction.

Compared with the current preoperative imaging modalities (ultrasonography, MRI, CT) and intraoperative imaging techniques (ultrasonography), our studies show that intraoperative ICG-based NIR-I/II fluorescence imaging can detect the tumour lesions with no obvious imaging characteristics (Supplementary Table 7, Figs. 3 and 4, and Supplementary Fig. 3). After laparotomy, intraoperative NIR-I/II fluorescence imaging was able to detect the lesions missed by preoperative imaging modalities, which can substantially promote the accuracy of patient staging and management (Fig. 3). During surgery, NIR-I/II imaging can also identify residual lesions that are difficult to be recognized by surgeons or intraoperative ultrasonography (Fig. 4). Moreover, our imaging study revealed that ICG distributed quite uniformly in well-differentiated or moderately differentiated tumours, but partial-type and rim-type distributions were found in the poorly differentiated HCCs (Supplementary Fig. 5), which is consistent with previously reported findings³⁷.

However, using ICG for NIR-I/II fluorescence imaging has some limitations. In this study, ICG was selected for liver-cancer NIR-II imaging in patients because of its established use in the clinic. However, ICG is a non-targeted probe with suboptimal emission characteristics for NIR-II detection. It cannot distinguish malignant tumours from benign ones, and its accumulation in other tissues may lead to false positives (Table 1). It is expected that the performance of NIR-II imaging can be further improved with targeted probes that are purpose designed. Several IRDye800CW-based probes are able to generate NIR-II fluorescence, although they are currently applied to NIR-I imaging. These dyes could be conjugated with tumour-targeted biomolecules (such as monoclonal antibodies or peptides) and used for NIR-II tumour imaging with the NIR-I/II multispectral imaging system. Targeted fluorescent probes for NIR-II imaging could thus broaden the use of the multispectral imaging system for the detection of cancer and other diseases.

In summary, we have developed and applied an integrated visible and NIR-I/II multispectral imaging instrument with high detection sensitivity and resolution for the intraoperative NIR-II imaging of patients with cancer. Our study shows that NIR-II imaging has advantages over traditional NIR-I imaging in clinical scenarios, and thus highlights the promising clinical potential of intraoperative NIR-II fluorescence imaging and NIR-II image-guided surgery.

Methods

Study design. The goals of this study were to: (1) develop an integrated visible and NIR-I/II multispectral imaging instrument and technique for intraoperative fluorescence imaging and image-guided cancer surgery of patients; and (2) compare the NIR-II fluorescence imaging of the patients with NIR-I fluorescence imaging. We optimized the performance of the multispectral instrument, including the working distance, surgical field of view, imaging resolution, sensitivity and so on. Then, we demonstrated the feasibility of using the instrument to image HepG2 tumours and guide the tumour resection on mice. This pilot study of NIR-I/NIR-II imaging in patients with liver cancer has also been explored in a clinical trial (ChiCTR1900022453) in China.

Development of integrated visible and NIR-I/II multispectral imaging instrument and image processing program. The optical-imaging instrument consists of two sets of laser excitation equipment and the combined NIR-I/II and visible light imaging instrument. The NIR-II imaging subsystem is composed of a high-sensitivity InGaAs charge-coupled device (NIRvana 640, Teledyne Princeton Instruments) camera and lens (EF 24–70 mm F/2.8L II USM, Canon), connecting through an adapter that integrates an optical filter (1,000 nm LP, FEL1000, Thorlabs). The NIR-I imaging subsystem is composed of a high-sensitivity complementary metal–oxide–semiconductor (CMOS, PCO.edge 5.5m, PCO AG) and lens (EF 24–70 mm F/2.8L II USM, Canon). The lens and a filter (832 ± 18.5 nm BP, FF01-832/37, Semrock) are coupled with the CMOS camera using an adapter. Similarly, the visible imaging subsystem is made of a high-resolution colour-light CMOS camera (PCO.edge 5.5c, PCO AG) and a lens (EF 24–70 mm F/2.8L II USM, Canon). The excitation equipment includes the laser, optical fibre and beam expander. When the multispectral imaging instrument was operating, a 785 nm and 808 nm laser (output power 2.0 W, MW-GX-785 and MW-

GX-808, Changchun Leirui Optoelectronic Technology) were employed as the excitation source for NIR-I and NIR-II imaging, respectively. The three subsystems operate independently from each other, to reduce the potential mutual interference and provide desirable performance in each spectrum range. A thermoelectric (Peltier) cooling method was adopted for all the subsystems, which conducted with high compatibility and little disturbance. Images of NIR-I, NIR-II and visible light were acquired in a parallel manner. The detailed information related to optics is presented in Supplementary Table 1.

A program was specially designed based on MATLAB (MathWorks) to pseudo-colour the fluorescence images intraoperatively. In this program, original images were firstly de-noised through median filtering (neighbourhood size 9×9). Then, fluorescence images were converted into pseudo-coloured according to pixel counts. High-intensity areas were shown with yellow, while blue represented low intensity. Moreover, a visualization threshold indicating signal intensity of normal tissues was intraoperatively assigned on the basis of surgeon diagnosis. Pixel counts above this threshold were pseudo-coloured, while the below part was identified as normal tissue signal and turned into transparent. The threshold could be adjusted for satisfying demands in different surgeries.

After acquisition of fluorescence and visible light images (NIR-II with LightField 6, Teledyne Princeton Instruments; NIR-I and visible light with Camware 4, PCO AG), the developed MATLAB program was immediately employed to generate pseudo-coloured results that presented the fluorescence intensity distribution. The generated pseudo-coloured results were overlaid on the white-light tissue images. Then, the surgeons were able to readily recognize the location of tumours and determine resection areas.

Phantom imaging study. To compare the penetration depth and resolution of NIR-I/II imaging, chicken breast tissues with various thicknesses were used to cover the capillary glass tubes ($n = 3$ per group) containing ICG (25 mg per kit, Dandong Yichuang Pharmaceutical, this product was approved for clinical use by China Food and Drug Administration) dissolved in FBS. The thicknesses used were: 1.0, 2.0, 3.0, 4.0, 5.0, 6.0, 7.0, 8.0 and 9.0 mm. Then, NIR-I/II fluorescence images were acquired. The relationships between the depth of the sources and the signal intensities or SBR were investigated.

In vivo mice imaging study. To study the feasibility of the multispectral imaging instrument for detecting and guiding resection of tumours, subcutaneous HepG2 carcinoma mouse models were established by the tumour-block transplant method. The HepG2 cell line and female athymic nude mice ($n = 6$ biologically independent animals, 4–6 weeks old, weight 17–25 g) were obtained from the Department of Experimental Animals (Academy of Military Medical Sciences). To establish mouse models, HepG2 tumour obtained from an orthotopic mouse model was split into several small blocks, and each block was approximately 2 mm^3 . With isoflurane (RWD Life Science) anaesthetization, the mice received skin incision in the left front flank. Then a HepG2 block was implanted subcutaneously through the incision to each mouse, followed by incision closure. Povidone-iodine was used to disinfect during tumour model establishment. When tumours reached 7 mm in diameter around 20 d later, the HepG2 tumour-bearing mice ($n = 3$ biologically independent animals per group) were subjected to in vivo imaging studies. First, the mice were injected with ICG (0.1 mg ml^{-1} , 0.1 ml, diluted with sterile water for injection) through the tail vein, and at 24 h, the mice received NIR-II and NIR-I imaging for tumour detection and then NIR-II and NIR-I fluorescence image-guided tumour resection. A 500 ms exposure time was used for NIR-II imaging, while 300 ms exposure was used to acquire NIR-I images. The excitation laser power was $30\text{--}35 \text{ mW cm}^{-2}$. The excised tumour tissue was subjected to histopathological examination. All animal studies were approved by the Institutional Animal Care and Use Committee, Chinese Academy of Sciences. All procedures were carried out strictly in accordance with the appropriate institutional guidelines for animal research.

Patient characteristics. Patients were recruited from the Affiliated Hospital of Southwest Medical University in China between October 2017 and July 2018. Twenty-three patients with liver cancer were considered eligible for the study. Preoperative imaging modalities including CT, MRI, ultrasonography and PET were used to diagnose liver cancer (detailed information is provided in the Supplementary Information). Other inclusion criteria included an age of 18 years or older and written informed consent. Exclusion criteria were patient experience of claustrophobia, pregnancy or lactation. This study was approved by the Medical Ethics Review Committee of the Affiliated Hospital of Southwest Medical University and was registered at ChiCTR.org.cn. Baseline characteristics of all patients are shown in Supplementary Table 2. Surgical procedures were determined according to the American Joint Committee on Cancer (AJCC) liver-cancer resection standard and an ICG 15 min retention rate.

NIR-I/II imaging studies of patients. ICG (2.5 mg ml^{-1} , diluted with sterile water for injection) with a dose of 0.5 mg kg^{-1} body weight was injected intravenously within 1–7 d (mean 3.74 and median 4) before the surgery. In the operating room, after the laparotomy, the visual inspection, manual palpation and intraoperative ultrasonography (Pro Focus 2202, BK Medical) were first performed to examine

whether there were any other metastatic tumours in the abdominal cavity. Liver tissues within 5 cm distance from the preoperatively detected lesion first received intraoperative ultrasonography. Then, the right hepatic lobe, left hepatic lobe, caudal hepatic lobe, hepatoduodenal ligament and other abdominal organs were scanned in sequence by intraoperative ultrasonography. In the right lobe, hepatic segments of S5, S8, S6 and S7 were successively scanned. In the left lobe, hepatic segments were scanned in the sequence S4, S2 and S3. Hepatic segment S1 was scanned in the caudal hepatic lobe. Any abnormal lesions detected by intraoperative ultrasonography were recorded. Subsequently, intraoperative *in vivo* NIR-I and NIR-II fluorescence imaging were used to examine the liver surface using the multispectral imaging instrument. An exposure time of 500 ms was set for NIR-II imaging, 300 ms for NIR-I imaging and 50 ms for visible imaging. The laser power for excitation was 30–50 mW cm⁻² during NIR-I/II imaging. Illumination for visible imaging was provided by 28 W sunlight lamps installed on the ceiling of the surgery room.

For tumours detected by intraoperative *in vivo* NIR-I/II imaging, intraoperative ultrasonography was combined to confirm its depth, size and characteristics. The tumour was removed by the guidance of NIR-I fluorescence images. After resection, *in vivo* NIR-I and NIR-II fluorescence imaging were employed to determine whether there were residual lesions in the patient. The TNR was calculated as a parameter for the *in vivo* imaging study. The malignant tumour-detection rate was calculated, which was defined as the ratio of the malignant tumour number detected by ICG fluorescence imaging, including from both operative and resected fields, to the number of malignant tumours verified and detected by H&E examination.

Patient safety was assessed and graded according to the Common Terminology Criteria for Adverse Events (AE, version 5.0)³⁶ by monitoring vital signs and performing routine blood tests. Within the first 24 h after ICG injection, the research team kept in phone contact with each patient, monitoring for potential AE responses. We noted and analysed any possible side effects during the week following intraoperative NIR-I/II imaging.

NIR-I/II imaging studies in resected specimens. After tumour resection, the resected specimens were transversely incised along the maximum tumour diameter on the basis of surgeon diagnosis. Then, the specimens were further sliced into several pieces with a thickness of approximately 10 mm. Each of the tissue sections received intraoperative *ex vivo* NIR-I/II imaging, to detect all the tumour lesions. Lastly, tumour lesions underwent routine histopathological examination procedures. NIR-I/II fluorescence images were compared with the gold-standard H&E stained images. The TNR was also calculated as a parameter to the resected tissue along with normal liver tissue, and the TBR was used for the tumour specimen without normal liver tissue. Fluorescence from black paper, placed underneath the resected tissue, was used as the background.

Statistical analysis. To investigate the relationship between the NIR-II and NIR-I imaging, a two-sided Welch's *t*-test was employed to compare the quantitative data between two independent samples. Quantitative results are expressed as mean ± s.d.).

Reporting Summary. Further information on research design is available in the Nature Research Reporting Summary linked to this article.

Data availability

The main data supporting the results in this study are available within the paper and its Supplementary Information. The raw and analysed datasets are available in figshare with the identifier <https://doi.org/10.6084/m9.figshare.10316318> (ref. ³⁹).

Code availability

Custom-developed code was applied to overlay the fluorescence signals on photographs. The raw MATLAB codes are available from the corresponding author upon request.

Received: 11 March 2019; Accepted: 22 November 2019;

Published online: 23 December 2019

References

- James, M. L. & Gambhir, S. S. A molecular imaging primer: modalities, imaging agents, and applications. *Physiol. Rev.* **92**, 897–965 (2012).
- Vahrmeijer, A. L., Hutteman, M., van der Vorst, J. R., van de Velde, C. J. & Frangioni, J. V. Image-guided cancer surgery using near-infrared fluorescence. *Nat. Rev. Clin. Oncol.* **10**, 507–518 (2013).
- Vinegoni, C. et al. Indocyanine green enables near-infrared fluorescence imaging of lipid-rich, inflamed atherosclerotic plaques. *Sci. Transl. Med.* **3**, 84ra45 (2011).
- Choi, H. S. et al. Targeted zwitterionic near-infrared fluorophores for improved optical imaging. *Nat. Biotechnol.* **31**, 148–153 (2013).
- Tichauer, K. M. et al. Microscopic lymph node tumor burden quantified by macroscopic dual-tracer molecular imaging. *Nat. Med.* **20**, 1348–1353 (2014).
- Pan, Y. et al. Endoscopic molecular imaging of human bladder cancer using a CD47 antibody. *Sci. Transl. Med.* **6**, 260ra148 (2014).
- Miller, J. et al. Perfusion-based fluorescence imaging method delineates diverse organs and identifies multifocal tumors using generic near-infrared molecular probes. *J. Biophoton.* **11**, e201700232 (2018).
- van Manen, L. et al. A practical guide for the use of indocyanine green and methylene blue in fluorescence-guided abdominal surgery. *J. Surg. Oncol.* **118**, 283–300 (2018).
- Tipirneni, K. E. et al. Oncologic procedures amenable to fluorescence-guided surgery. *Ann. Surg.* **266**, 36–47 (2017).
- Hutteman, M. et al. Randomized, double-blind comparison of indocyanine green with or without albumin premixing for near-infrared fluorescence imaging of sentinel lymph nodes in breast cancer patients. *Breast Cancer Res. Treat.* **127**, 163–170 (2011).
- Gurtner, G. C. et al. Intraoperative laser angiography using the SPY system: review of the literature and recommendations for use. *Ann. Surg. Innov. Res.* **7**, 1 (2013).
- Koller, M. et al. Implementation and benchmarking of a novel analytical framework to clinically evaluate tumor-specific fluorescent tracers. *Nat. Commun.* **9**, 3739 (2018).
- Van Dam, G. M. et al. Intraoperative tumor-specific fluorescence imaging in ovarian cancer by folate receptor- α targeting: first in-human results. *Nat. Med.* **17**, 1315–1319 (2011).
- Burggraaf, J. et al. Detection of colorectal polyps in humans using an intravenously administered fluorescent peptide targeted against c-Met. *Nat. Med.* **21**, 955–961 (2015).
- Rosenthal, E. L. et al. Sensitivity and specificity of cetuximab-IRDye800CW to identify regional metastatic disease in head and neck cancer. *Clin. Cancer Res.* **23**, 4744–4752 (2017).
- He, S., Song, J., Qu, J. & Cheng, Z. Crucial breakthrough of second near-infrared biological window fluorophores: design and synthesis toward multimodal imaging and theranostics. *Chem. Soc. Rev.* **47**, 4258–4278 (2018).
- Hong, G., Antaris, A. L. & Dai, H. Near-infrared fluorophores for biomedical imaging. *Nat. Biomed. Eng.* **1**, 0010 (2017).
- Dang, X. et al. Layer-by-layer assembled fluorescent probes in the second near-infrared window for systemic delivery and detection of ovarian cancer. *Proc. Natl Acad. Sci. USA* **113**, 5179–5184 (2016).
- Hong, G. et al. Multifunctional *in vivo* vascular imaging using near-infrared II fluorescence. *Nat. Med.* **18**, 1841–1846 (2012).
- Robinson, J. T. et al. *In vivo* fluorescence imaging in the second near-infrared window with long circulating carbon nanotubes capable of ultrahigh tumor uptake. *J. Am. Chem. Soc.* **134**, 10664–10669 (2012).
- Hong, G. et al. Near-infrared II fluorescence for imaging hindlimb vessel regeneration with dynamic tissue perfusion measurement. *Circ. Cardiovasc. Imaging* **7**, 517–525 (2014).
- Sun, Y. et al. Novel benzo-bis(1,2,5-thiadiazole) fluorophores for *in vivo* NIR-II imaging of cancer. *Chem. Sci.* **7**, 6203–6207 (2016).
- Zhang, X. D. et al. Traumatic brain injury imaging in the second near-infrared window with a molecular fluorophore. *Adv. Mater.* **28**, 6872–6879 (2016).
- Wang, R., Zhou, L., Wang, W., Li, X. & Zhang, F. *In vivo* gastrointestinal drug-release monitoring through second near-infrared window fluorescent bioimaging with orally delivered microcarriers. *Nat. Commun.* **8**, 14702 (2017).
- Cheng, K. et al. Synthesis, characterization, and biomedical applications of a targeted dual-modal near-infrared-II fluorescence and photoacoustic imaging nanoprobe. *ACS Nano* **11**, 12276–12291 (2017).
- Wan, H. et al. A bright organic NIR-II nanofluorophore for three-dimensional imaging into biological tissues. *Nat. Commun.* **9**, 1171 (2018).
- Antaris, A. L. et al. A small-molecule dye for NIR-II imaging. *Nat. Mater.* **15**, 235–242 (2016).
- Sun, Y. et al. Novel bright-emission small-molecule NIR-II fluorophores for *in vivo* tumor imaging and image-guided surgery. *Chem. Sci.* **8**, 489–3493 (2017).
- Sun, Y. et al. Novel dual-function near-infrared II fluorescence and PET probe for tumor delineation and image-guided surgery. *Chem. Sci.* **9**, 2092–2097 (2018).
- Antaris, A. L. et al. A high quantum yield molecule-protein complex fluorophore for near-infrared II imaging. *Nat. Commun.* **8**, 15269 (2017).
- Carr, J. A. et al. Shortwave infrared fluorescence imaging with the clinically approved near-infrared dye indocyanine green. *Proc. Natl Acad. Sci. USA* **115**, 4465–4470 (2018).
- Starosolski, Z. et al. Indocyanine green fluorescence in second near-infrared (NIR-II) window. *PLoS ONE* **12**, e0187563 (2017).
- Gotoh, K. et al. A novel image-guided surgery of hepatocellular carcinoma by indocyanine green fluorescence imaging navigation. *J. Surg. Oncol.* **100**, 75–79 (2009).
- Ishizawa, T. et al. Real-time identification of liver cancers by using indocyanine green fluorescent imaging. *Cancer* **115**, 2491–2504 (2009).

35. Morita, Y. et al. Detection of hepatocellular carcinomas with near-infrared fluorescence imaging using indocyanine green: its usefulness and limitation. *Int. J. Clin. Oncol.* **18**, 232–241 (2013).
36. Ishizawa, T. et al. Mechanistic background and clinical applications of indocyanine green fluorescence imaging of hepatocellular carcinoma. *Ann. Surg. Oncol.* **21**, 440–448 (2014).
37. Shimada, S., Ohtsubo, S., Ogasawara, K. & Kusano, M. Macro- and microscopic findings of ICG fluorescence in liver tumors. *World J. Surg. Oncol.* **13**, 198 (2015).
38. *Common Terminology Criteria for Adverse Events (CTCAE) Version 5.0* (US Department of Health and Human Services, 2017); https://ctep.cancer.gov/protocolDevelopment/electronic_applications/docs/CTCAE_v5_Quick_Reference_8.5x11.pdf
39. Hu, Z. et al. Dataset for first-in-human liver tumour surgery guided by multispectral fluorescence imaging in the visible and near-infrared-I/II windows. *figshare* <https://doi.org/10.6084/m9.figshare.10316318> (2019).

Acknowledgements

This study was supported by the National Key Research and Development Program of China (2017YFA0205200, 2016YFC0102600), National Natural Science Foundation of China (NSFC) (81930053, 61622117, 81671759, 81227901), the Chinese Academy of Sciences (GJJSTD20170004), Beijing Natural Science Foundation (JQ19027), Beijing Nova Program (Z181100006218046), the Scientific Instrument Developing Project of the Chinese Academy of Sciences (YZ201672), the innovative research team of high-level local universities in Shanghai, and the Zhuhai High-level Health Personnel Team Project (Zhuhai HLHPTP201703). We acknowledge the instrumental and technical support of

the multi-modal biomedical imaging experimental platform, Institute of Automation, Chinese Academy of Sciences.

Author contributions

J.T., Z.C. and Z.H. conceived the idea of the project. Z.H. wrote the manuscript in addition to designing, performing and analysing all experiments. Z.H., C.F., B.L. and Z.Z. performed the experiments. S.S., P.H. and X.X. collected the information on patients with liver cancer. X. Sun., T.Z. and Y.Z. assisted with histology. Y.C. assisted with PET/CT imaging. C. Cao., M.C., X. Shi., C.L. and C. Chi. assisted with data analysis. Z.C. and S.S.G. assisted with experimental design, manuscript preparation and data/image analysis. J.T. designed, supervised and analysed all experiments, in addition to assisting with manuscript preparation.

Competing interests

The authors declare no competing interests.

Additional information

Supplementary information is available for this paper at <https://doi.org/10.1038/s41551-019-0494-0>.

Correspondence and requests for materials should be addressed to S.S.G., Z.C. or J.T.

Reprints and permissions information is available at www.nature.com/reprints.

Publisher's note Springer Nature remains neutral with regard to jurisdictional claims in published maps and institutional affiliations.

© The Author(s), under exclusive licence to Springer Nature Limited 2019